Available online at

jae.cardiffuniversitypress.org

ISSN 2752-7735
The Journal of Ammonia Energy 03 (2025) 042–053

An experimental and numerical investigation of a liquid ammonia jet flame: spray characteristics close to nozzle and flame structure

Zhenhua An[a], Ruixiang Wang[a], Jiangkuan Xing[a,*], Meng Zhang[b], Ryoichi Kurose[a]

[a] *Department of Mechanical Engineering and Science, Kyoto University, Kyoto daigaku-Katsura, Nishikyo-ku, Kyoto 615-8540, Japan*
[b] *State Key Laboratory of Multiphase Flow in Power Engineering, Xi'an Jiaotong University, Xi'an 710049, China*

Abstract

Liquid ammonia combustion has become a focal point in current ammonia combustion research due to its potential to simplify fuel supply systems, reduce costs, and improve the responsiveness of combustion systems. In this study, the spray characteristics of liquid ammonia close to the nozzle and jet flame structure are experimentally and numerically investigated. The spray characteristics of liquid ammonia generated using an ammonia piloted jet spray burner (AJSB) are measured using Particle/Droplet Image Analysis (PDIA). The liquid ammonia jet flame structure is further analyzed using a quasi-carrier-phase Direct Numerical Simulation (quasi-DNS) coupled with a detailed chemistry under the Euler-Lagrangian framework. The experimental results indicate that the liquid ammonia undergoes flash boiling inside the injection tube, with only 22.8% of the ammonia remaining in the liquid state after injection, and the atomized droplets have an average diameter of less than 40 μm. On the other hand, the quasi-DNS results show that flash evaporation leads to a low axial flame temperature, with droplets confined to the low-temperature region and almost completely evaporating before reaching the flame front. In addition, the results indicate that the expansion of the reaction zone in the liquid ammonia jet flame is a process that develops spatially from upstream to downstream while being influenced by the interactions between local eddies and the flame. This behavior is consistent with the findings reported in gaseous ammonia jet flames, a similarity attributed to the characteristics of liquid ammonia flash evaporation, resulting in combustion characteristics similar to those of gaseous ammonia.

Received: 29th Nov 24; Accepted: 10th Feb 25; Published: 11th April 25

Keywords: Liquid ammonia, Ammonia combustion, Jet flame, quasi-DNS, Detailed chemistry.

1. Introduction

In order to achieve the goal of reducing carbon emissions and sustainable energy use, the combustion of ammonia, as one of the alternative energy, hydrogen carriers, and carbon free fuels, has recently received increasing attention [1]. Because of the well-established infrastructure for ammonia storage and transport, ammonia has broad prospects in the long-term goal of reducing carbon emissions. Remarkable progress has been made on gaseous ammonia in recent decades [2–4]. Extensive basic and applied research has been conducted on the combustion of ammonia. For instance, studies focusing on the fundamental combustion properties of ammonia [5,6], ammonia/methane [7,8], and ammonia/hydrogen [9–11] flames, have been progressed. Additionally, the application of ammonia in various engineering systems, including internal combustion engines (ICEs) and gas turbines (GTs), has been explored through numerous experimental [12,13] and simulation [6,14] investigations.

These studies have mainly focused on the combustion of gaseous ammonia and mixtures of gaseous ammonia with methane or hydrogen. Ammonia is usually stored in the liquid phase, then direct combustion of liquid ammonia can reduce the cost and complexity of fuel supply systems for engineering devices [15], which reduces about 7 - 9% of the consumption of generated power for the vaporization process and the start-up time in gas turbines [16]. However, given that liquid ammonia combustion is a relatively emerging research area, studies related to this topic remain insufficient. Over the past three years, experimental research has primarily focused on spray dynamics within internal combustion engines [17–19], conducting measurements of spray morphology, penetration distance, and spray angle. Additionally, studies on dual-fuel combustion using liquid ammonia and diesel for ICEs have been undertaken [20–22]. In the context of gas turbines, preliminary experimental

---

* Corresponding author. Tel.: +81-090-7738-0834. E-mail address: xing.jiangkuan.6h@kyoto-u.ac.jp

https://doi.org/10.18573/jae.39

and numerical simulations of liquid ammonia swirl combustion have been carried out [16], identifying preheating temperature as a critical factor for enhancing combustion stability. Regarding numerical simulations, numerous spray modeling studies have been performed to date [23–26]. Following improvements to the phase change model, the Euler-Lagrangian framework-based methods can effectively capture the characteristics of liquid ammonia sprays.

However, relatively little effort has been devoted to the study of liquid ammonia jet flames. It is essential to analyze its spray and combustion characteristics. As a novel liquid fuel, the turbulent combustion dynamics of liquid ammonia jet flames, which involve the interplay of flash boiling, heat loss, mass transfer, reaction thermal chemistry, and flame surfaces, have not been fully understood and explored. Therefore, the aim of the present study is to establish a liquid ammonia jet flame in laboratory-scale burner, measure the spray characteristics close to nozzle, and perform a quasi-Direct Numerical Simulation (quasi-DNS) with detailed chemistry to investigate the spray characteristics and flame structure of the liquid ammonia jet flame. To the best of the authors' knowledge, this is the first study to combine experimental measurements and numerical simulations to analyze liquid ammonia jet flames.

The remainder of this paper is organized as follows. Section 2 presents the configuration of the target flame and the experimental methodologies employed. Section 3 details the numerical simulation methods. Section 4 discusses the results, beginning with an experimental analysis of the ammonia spray characteristics to provide key parameters for the simulation. The simulation results are subsequently validated against experimental data, followed by an examination of flame structure and the reaction zone. Finally, Section 5 concludes with a summary of the results.

2. Target flame and experimental methodologies

2. 1 Burner and experimental condition

A liquid ammonia jet flame is achieved in the ammonia piloted jet spray burner (AJSB) [27]. Figure 1 (a) shows the digital image of the liquid ammonia jet flame from experiment. The center of the burner is a liquid ammonia jet, surrounded by a co-flame of methane with the theoretical flame temperature of around 2,140 K. The ammonia jet flame is yellow in color, and the yellow chemiluminescence is caused by the $NH_{2\alpha}$ band spectrum [28]. Mie scattering laser shows the morphology of the liquid ammonia spray. Figure 1 (b) shows the schematic diagram of the AJSB. Liquid ammonia is injected through the center tube (shown as red) with a diameter of 1.27 mm. A coaxial air tube (shown as green) with a diameter of 4.62 mm surrounds the ammonia fuel tube. The exit of the fuel tube is lower than that of the air tube. The length is defined as the recess length, Lr. The Lr in this study is 6.5 mm, which is designed to ensure the presence of a certain proportion of liquid ammonia droplets. This Lr allows the liquid ammonia to undergo primary breakup under the outlet of the fuel pipeline, with the resulting droplets being carried into the computational domain by the carrier gas, a mixture of pre-evaporated ammonia and air. This setup enhances the comparability between the simulation and experimental results. Atomization will occur in this region before the exit of the air tube.

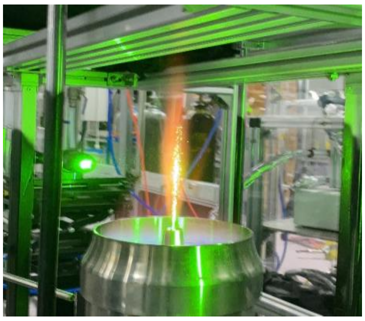
(a)

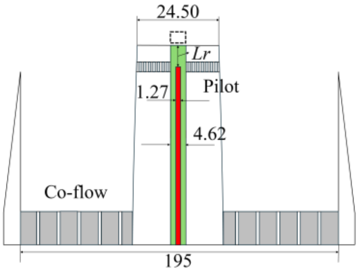

(b)

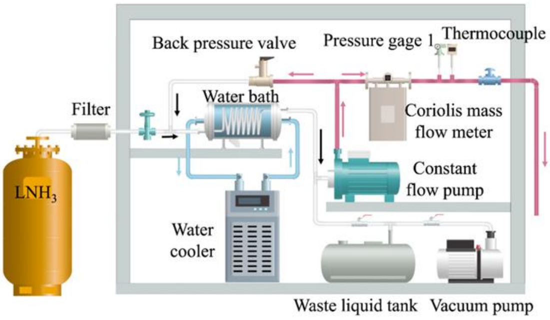

(c)

Fig. 1. (a) Digital image of the liquid ammonia jet flame from experiment. Mie scattering laser shows the morphology of liquid ammonia spray. (b) Schematic diagram of AJSB, and the unit is mm. (c) Schematic diagram of the liquid ammonia supply system.

After the liquid phase passes through the outlet of the air tube, the fully atomized spray is formed. The mean velocity of the main air jet is 67.57 m/s with a temperature of 235 K. The co-flow is used to ignite the fresh mixture, and the co-flow provides a hot atmosphere and stabilizes the jet flame. The co-flow is the burnt gas of methane/air with an equivalence ratio of 0.9. The velocity is 1 m/s. The details of the experimental condition are described in Table 1. The dashed black box represents the measurement window range of the Particle/Droplet Image Analysis (PDIA) experiment, which will be introduced in Section 2.2.

2. 2 Experimental methodologies

Liquid ammonia was supplied using a fuel supply system, which consists of a liquid fuel tank, pressurizer, water chiller, and a Coriolis mass flow meter. The detailed description of the fuel supply system can be found in our previous study [29]. Liquid ammonia with a purity exceeding 99.9% was pumped from the fuel tank to the pipeline, and passed through a water bath maintained at 268 K, and the pressure was increased to 1.8 ± 0.02 MPa using a constant flow pump to ensure liquid ammonia remained in liquid phase. Then, liquid ammonia was injected through the fuel tube.

The PDIA system was used to measure the microscopic characteristics of the spray. A single pulse laser was generated by the aforementioned laser source at 532 nm with an energy of 300 mJ. Then the laser is expanded to a uniform parallel light beam. The droplets in the camera's focal plane were illuminated by the laser and recorded by the same CCD camera, which was fitted with a long-focus microscope. The measurement window, calibrated using a scaling plate with a precision of 25 μm, measured 3.9 mm × 2.9 mm. The position of the measurement window was precisely controlled by moving the CCD camera using a motorized positioning system with 1 μm accuracy.

Table 1. Summary of target flame conditions.

Description	Value [unit]
Primary jet	
Global equivalence ratio, ϕ	1.0 [-]
Mass flow of liquid ammonia,	0.25 [g/s]
Volume flow of air	70 [L/min]
Recess length, Lr	6.5 [mm]
Inlet temperature, T_{in}	235 [K]
Ambient pressure, P_{ab}	1 [atm]
Mean velocity of air, U_{air}	67.57 [m/s]
Co-flame (Methane flame)	
Equivalence ratio, ϕ_{co}	0.9 [-]
Mean velocity, U_{co}	1 [m/s]

3. Numerical methodologies

3. 1 Governing equations

The transport equations for mass, momentum, species, and sensible enthalpy for gaseous phase are described without any filter by Eqs. (1) - (4), respectively.

$$\frac{\partial \rho}{\partial t} + \nabla\cdot(\rho\mathbf{u}) = \dot{S_\rho}\,, \tag{1}$$

$$\frac{\partial(\rho\mathbf{u})}{\partial t} + \nabla\cdot(\rho\mathbf{uu}) = -\nabla p + \nabla\cdot\boldsymbol{\tau} + \rho\mathbf{g} + \dot{\mathbf{S_u}}\,, \tag{2}$$

$$\frac{\partial(\rho h)}{\partial t} + \nabla\cdot(\rho\mathbf{u}h) = \frac{\partial p}{\partial t} + \mathbf{u}\cdot\nabla p + \nabla\cdot(\rho D_h\nabla h) + \boldsymbol{\tau}:\nabla\mathbf{u} + \dot{S}_{reac} + \dot{S}_h + \dot{S}_{rad}\,, \tag{3}$$

$$\frac{\partial(\rho Y_i)}{\partial t} + \nabla\cdot(\rho\mathbf{u}Y_i) = \nabla\cdot(\rho D_i\nabla Y_i) + \dot{S}_{evap,NH_3} + \dot{S}_{comb,i}\,, \tag{4}$$

where, ρ is the density, and u is the gaseous phase velocity vector. $\dot{S_\rho}$ represents the mass source term contributed from droplets. p is the hydrodynamic pressure, $\boldsymbol{\tau}$ is the viscous stress tensor, and h is the sensible enthalpy. D_h and D_k are the thermal diffusivity and mass diffusivity, respectively. The transport properties are considered using a mixture-averaged method. Y_k is the mass fraction of species k. $\dot{S}_{reac}$ and $\dot{S}_h$ in Eq. (3) are the heat source terms for reaction and evaporation, respectively. $\dot{S}_{evap,NH_3}$ and $\dot{S}_{comb,i}$ in Eq. (4) represent the mass source terms originated from evaporation and combustion, respectively. These source terms take into account the interaction between the gaseous and dispersed phases using two-way coupling particle-source-in-cell (PSIC) method [30] between both the phases as follows,

$$\dot{S_\rho} = -\frac{1}{\Delta V}\sum_i^N \frac{dm_d}{dt}\,, \tag{5}$$

$$\dot{\mathbf{S_u}} = -\frac{1}{\Delta V}\sum_i^N \frac{dm_d\mathbf{u}_d}{dt}\,, \tag{6}$$

$$\dot{S}_h = -\frac{1}{\Delta V}\sum_i^N \frac{d(c_p m_d T_d)}{dt}\,, \tag{7}$$

$$\dot{S}_{evap,NH_3} = -\frac{1}{\Delta V}\sum_i^N \frac{dm_d}{dt}\,, \tag{8}$$

where ΔV is the volume of the computational grid cell within which a certain ammonia droplet resides, and N is the number of ammonia droplets within a given computational grid cell. m_d, u_d, and h_d are droplet mass, velocity, and specific enthalpy of an ammonia droplet, respectively. In this study, the maximum value of droplet diameter is smaller than the grid size, which meets the conditions for using the PSIC method [31].

The multi-phase flow is calculated through the two-way coupled Eulerian–Lagrangian formulation, and each Lagrangian droplet is governed by Miller et al.

[35]. The equations of droplets' position, velocity, and temperature are solved by Eqs. (9) - (11), respectively.

$$\frac{d\mathbf{x}_{d,i}}{dt} = \mathbf{u}_{d,i} \,, \tag{9}$$

$$\frac{dm_d\mathbf{u}_{d,i}}{dt} = m_d \frac{3\mu C_D Re}{4d^2\rho_d}\left(\mathbf{u}_i - \mathbf{u}_{d,i}\right) + m_d\mathbf{g}_i \,, \tag{10}$$

$$\frac{dT_d}{dt} = f h_t \frac{A_d}{mc_p}(T_\infty - T_d) - \frac{dm}{dt}h_v \,, \tag{11}$$

where $\boldsymbol{x}_{d,i}$, $\boldsymbol{u}_{d,i}$, T_d, and m_d are the droplet position, velocity, temperature, and mass, respectively. f_1 is the Stokes drag correction. $\tau_d = \rho_l d^2/(18\mu)$ is the droplet relaxation time; $\boldsymbol{g}_i$ represents the gravitational acceleration. The correction coefficient is,

$$f = \frac{-c_{p,v}\dot{m}}{\pi dkNu} \Big/ \left(e^{\frac{-c_{p,v}\dot{m}}{\pi dkNu}} - 1\right) \tag{12}$$

where $h_t = kNu/d$ is the heat transfer coeffcient, and k is the thermal conductivity. A_d is each droplet's surface area. $Nu = 2 + 0.6Re^{1/2}Pr^{1/3}$ is Nusselt number calculated using the Ranz Marshall heat transfer model [34]. dm_d/dt is calculated using a combined phase-change model, which has been validated under flash boiling conditions in our previous study [23].

Because the primary break-up happens within the Lr distance, it is not directly modelled. It is accounted for by employing the Rosin-Rammler (R-R) distribution law for the initial droplet diameter. The second break-up of the droplets was considered. In this study, the Reitz-Diwakar breakup model [35] was applied. There are two break-up categories: bag break-up and stripping break-up, and both of them are due to aerodynamic forces acting on the surface of the droplet. Weber number,

$$We=\rho|\boldsymbol{u}_{rel}|2D_{d,stable}/(2\delta_d), \tag{13}$$

is used to separate these two categories as follows:

$$\begin{cases} We > C_{\text{bag}} & \text{bagbreak} - \text{up} \\ We > Re^{0.5}C_{\text{strip}} & \text{strippingbreak} - \text{up} \end{cases}. \tag{14}$$

The break-up rate is calculated by,

$$\frac{dD_t}{dt} = \frac{D_d - D_{d,stable}}{\tau_b}, \tag{15}$$

where D_d and $D_{d,stable}$ are the instantaneous and the stable droplet diameters. τ_d is the break-up timescale. The values of stable droplet diameter and break-up timescale for these two kinds of break-up are calculated using the following equation. For bag break-up:

$$\frac{\rho|\boldsymbol{u}_{rel}|^2 D_{d,stable}}{2\delta_d} = We \geq C_{bag}, \tag{16}$$

$$\tau_b = \frac{C_b\rho_d^{1/2}D_d^{3/2}}{4\delta_d^{1/2}}. \tag{17}$$

For stripping break-up:

$$\frac{We}{\sqrt{Re}} \geq C_{strip}, \tag{18}$$

$$\tau_b = \frac{C_s}{2}\sqrt{\frac{\rho_d}{\rho}}\frac{D_d}{|\boldsymbol{u}_{ref}|}. \tag{19}$$

Where, $\boldsymbol{u}_{ref}$ is the relative velocity. We and Re are the Weber and Reynolds numbers. The values of stable droplet diameter and break-up timescale are calculated based on the empirical constants C_{bag}, C_b, C_{strip}, and C_s. The specific values of these empirical constants are referenced from the previous study of flash-boiling fuel sprays [36].

3. 2 Computational details

The simulation configuration is consistent with the experimental set-up. The process of atomization in the recess length was simplified in the simulation and accounted for using the R-R distribution for initial-droplet diameter. The details of droplet distribution will be introduced in Section 4.1. The break-up of the ammonia droplets is considered by incorporating appropriate models. The turbulence jet bulk velocity was generated using the pipe flow method. The fully developed velocity field on the cross-section of the pipe flow is mapped to the mainstream inlet for the ammonia jet. The jet of fully turbulent pipe flow carrying ammonia droplets was operated at atmospheric pressure. The temperature of the mainstream jet, T_{in} = 235 K, was measured by thermocouples. The mean velocity was calculated based on the volume flow rate of air, considering phase change. The Reynolds number for the primary jets is 25,036 based on the gaseous phase velocity. All configurations are consistent with the experimental setup.

The computational domain is shown in Fig. 2 with the size of 144 × 144 × 180 mm^3. The mesh at the center is refined and stretched in the radical and axial direction. In the reaction region, the grid size is smaller than the Kolmogorov length scale. The smallest Kolmogorov length scale in the reaction region is around 100 μm. And the grid resolution ensures that approximately ten grid points are present across the flame thickness. The total cell number is around 0.29 billion.

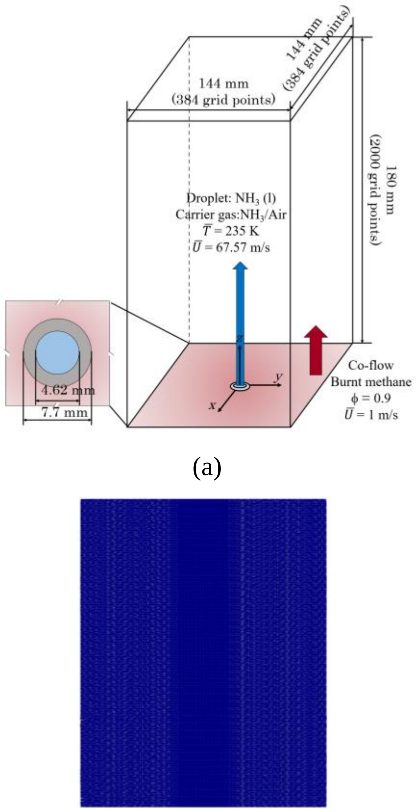

(a)

(b)

Fig. 2. (a) Schematic of computational domain and conditions for simulation, (b) meshing detail (*x-z* plane).

The simulation was carried out using a quasi-direct numerical simulation code developed based on OpenFOAM-8 [37]. A second-order central differencing scheme was used to integrate both spatial and transient terms. The Euler-implicit scheme was applied for integrating temporal terms. The pressure implicit split operator (PISO) algorithm [38] was employed to manage the coupling between pressure and velocity. The simulation was conducted on the supercomputer Fugaku, requiring approximately 1,400,000 core hours of parallel computation using 4,800 processers.

4. Results and Discussion

4. 1 Spray characteristics

Figure 3 shows the data processing for measuring the droplet diameter. It includes (a) the original grayscale image of droplets on a surface, displaying various sizes and some background elements. (b) The binary image, created using gradient information, depicts droplets as white shapes on a black background, emphasizing their edges. (c) The final image overlays red markings on the original image to highlight the detected boundaries of the droplets. Note that the position with the strongest gradient change in the image is usually the object on the focal plane. This process enhances the precision of droplet characterization by isolating them from the background and other visual noise, enabling detailed analysis of their spatial distribution and size.

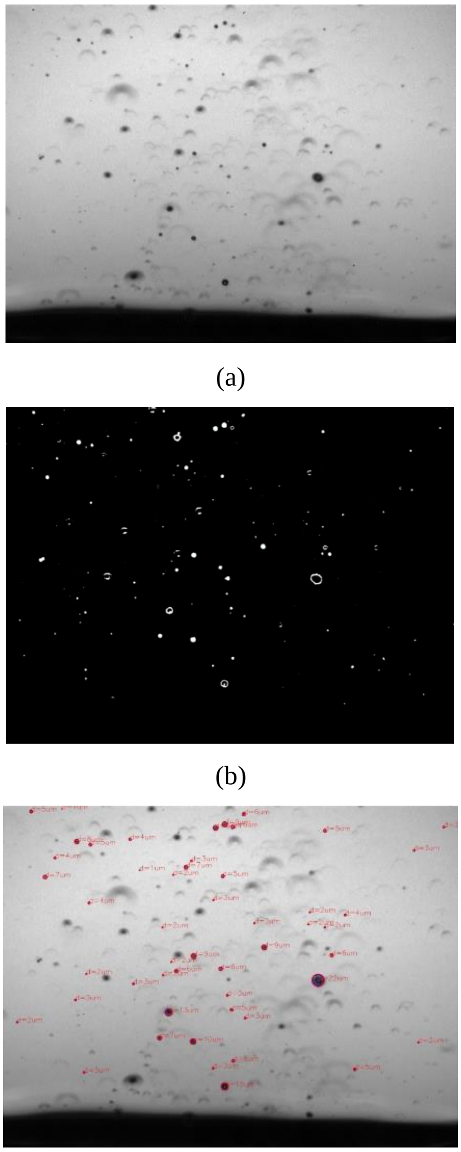

(a)

(b)

(c)

Fig. 3. Data processing flow for PDIA. (a) Original image, (b) Binary images drawn through gradient information, and (c) Droplet image.

After liquid ammonia is injected out of the fuel pipe, a complex phase transition process occurs within the *Lr* distance that includes atomization, evaporation, flash boiling, etc. A portion of the liquid ammonia will evaporate to gaseous phase. The percentage of non-evaporation droplets mass, $m_{NH3(l)}$, represents the percentage of liquid ammonia without pre-evaporation in the inlet tube. In this study, $m_{NH3(l)}$

was calculated using the liquid volume measured by PDIA. Figure 4 shows the statistical value of $m_{NH3(l)}$, which were collected over a duration of 30 seconds. The mean vale of $m_{NH3(l)}$ is 22.8%, which indicates that 77.2% of liquid ammonia has undergone a phase transition to a gaseous state in the *Lr* region. Therefore, the dilute-suspension assumption may be permitted for the droplet-laden flow, wherein the droplet–droplet interaction modeling becomes less important. The length of *Lr* significantly influences the proportion of pre-evaporated liquid ammonia, which will be investigated in future studies. Under the current condition of $Lr = 6.5$ mm, a substantial proportion of liquid ammonia undergoes phase transition to the gaseous state before reaching the outlet. In the experiments, a sharp temperature drop was observed near the nozzle, and prolonged injection resulted in frost formation. The unique characteristics of liquid ammonia flash boiling are markedly different from the pre-evaporation properties of traditional fuels such as ethanol and acetone [39,40].

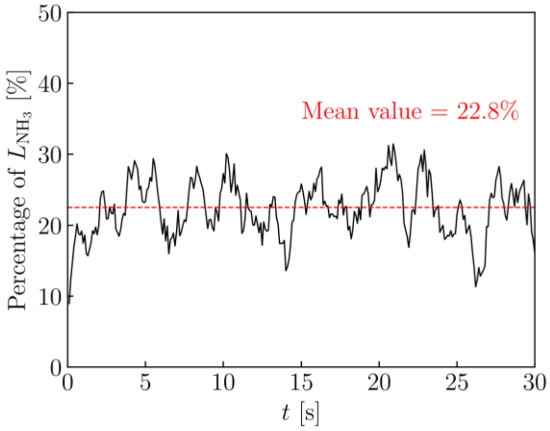

Fig. 4. Statistical variation of the percentage of un-evaporation droplets mass over the time.

The R-R distribution is used to describe the droplets diameter. There are four parameters, i.e., maximum and minimum value of droplets (d_{max} and d_{min}), shape parameter (n), and scale parameter (d). Table 2 shows the parameters of droplet inflow conditions. d_{max} and d_{min} were measured using PDIA system. The values of n and d are obtained by fitting the experimental data.

Table 2. Summary of droplet distribution.

Parameter	Value [unit]
d_{max}	80 [μm]
d_{min}	2.44 [μm]
n	1.25 [-]
d	13.5 [μm]

The distribution of droplets diameter between experimental measurement and the R-R parameter fitting is shown in Fig. 5. The blue dots represent the experimentally measured droplet distribution, while the black lines correspond to the droplet diameter distribution fitted using the R-R distribution. It can be seen that after the atomization caused by flash boiling, the majority of liquid ammonia droplets have diameters below 40 μm, with only a very small fraction of larger droplets present. The inlet conditions account for the phase change, where approximately 77.2% of liquid ammonia is converted into gaseous ammonia before the mixture gets into chamber. The mass fractions of NH3, O_2, and N_2 at the inlet boundary are carefully calculated to consider the pre-evaporation effect.

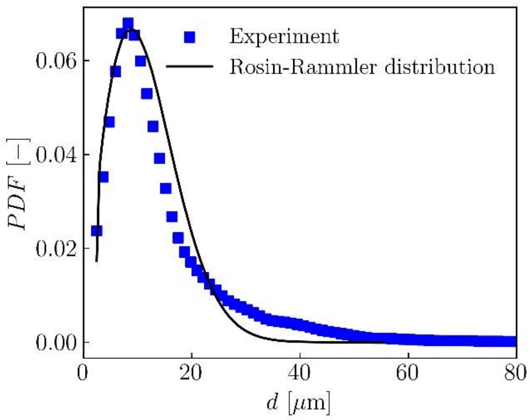

Fig. 5. Comparison of droplet size probability density function (PDF) of injected fuel droplets between experiment and R-R distribution.

4. 2 Validation

Figure 6 shows the comparison of instantaneous droplet distribution between the experiment employing global Mie scattering (left) and the present quasi-DNS (right). The measurement window of the experiment is 90 × 40 mm², and the size of the points represents the size of the droplets. The operating range is performed at two different axial positions, 0 mm and 20 mm. At each measurement position, 300 images were captured at a frequency of 10 Hz. Mie scattering measures the distribution of droplets on a cross-sectional plane. Therefore, the simulation corresponds to extracting the droplet distribution on the *x*-*z* longitudinal cross-section. These results show the same trend as the intensity decreases from upstream to downstream locations, which means the droplets continue to evaporate. The simulation underestimates the spray width downstream, with fewer droplets separating from the main flow compared to the experiment. However, the core region matches the experimental results well. There are several factors that may have contributed to the discrepancy. On the experimental side, minor fluctuations of liquid ammonia supplement and measurement uncertainties could have influenced the results. On the computational side, certain assumptions in the model, such as simplified boundary conditions or absence of atomization models, might have led to deviations from the experimental data.

In the experiment, the Sauter Mean Diameter (SMD) of droplets was measured within a viewing window of 3.9 × 2.9 mm² at the nozzle and 20 mm directly above the nozzle, as shown in Fig. 7. The blue line represents the simulated SMD of droplets along the axis. It can be observed that the simulation slightly underestimates the mean droplet diameter, primarily due to the following reasons: (1) The discrepancies between the experiment and simulation mainly arise from differences in sampling methods. In the experiment, SMD is calculated based on two-dimensional image data, while in the simulation, droplet statistics are collected across the entire three-dimensional space at different heights. (2) In reality, a certain degree of droplet coalescence occurs, leading to an increase in droplet size. However, this process is neglected in the simulation, resulting in a smaller predicted SMD compared to the experimental measurements.

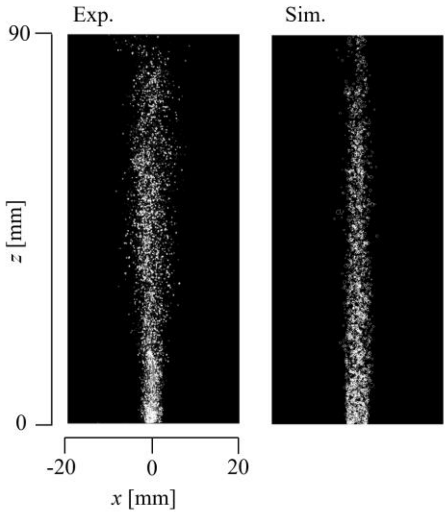

Fig. 6. Comparison of instantaneous liquid ammonia droplets distribution (*x*-*z* plane) between experiment (left) and simulation (right).

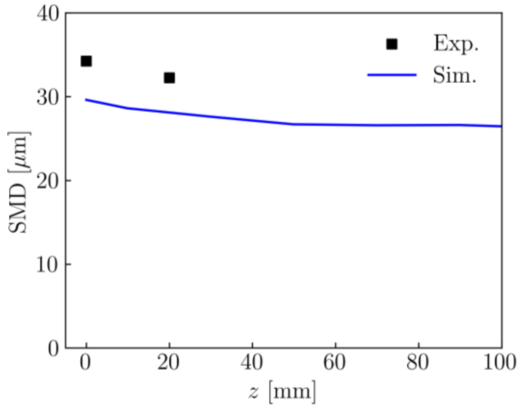

Fig. 7. Comparison of the SMD of droplets along the z-axis between experiment (black dots) and simulation (blue line).

4. 3 Flame structure

Figure 8 shows the instantaneous fields of liquid ammonia jet flame from the simulations. Figure 8 (a) illustrates the temperature field and droplet distribution of the liquid ammonia jet flame. Since the co-flow is supplied by the burned products of methane at an equivalence ratio of 0.9, its temperature remains higher than the peak combustion temperature of ammonia. As a result, there is no significant temperature rise in the temperature field. Ammonia reacts in a high-temperature, low-oxygen environment, representing a MILD combustion configuration [41], which will be explored in our future research. In the droplet region near the axis, the gas-phase temperature drops significantly, approaching 230 K, due to the substantial heat absorption from the flash evaporation of liquid ammonia. There is a pronounced temperature gradient from the axis to the burned region. Furthermore, the droplet distribution indicates that relatively larger droplets are primarily located in the upstream region. From upstream to downstream locations, the droplet diameter gradually decreases. However, due to the extremely low temperature in the droplet core region near the axis, some larger droplets still exist in the downstream region. These larger droplets are more likely to interact with the flame. Owing to the rapid flash evaporation rate of liquid ammonia, the majority of droplets completely evaporate before entering the burned region, making it challenging to observe droplets within the burned zone. Figure 8 (b) shows the mass fraction distribution of ammonia. Since around 80% of the liquid ammonia has already undergone phase transition within the recess length region, gaseous ammonia is present downstream. As the flow progresses downstream, the ammonia concentration gradually decreases, and by approximately z = 160 mm, ammonia is almost entirely consumed, with the droplets nearly completely evaporated.

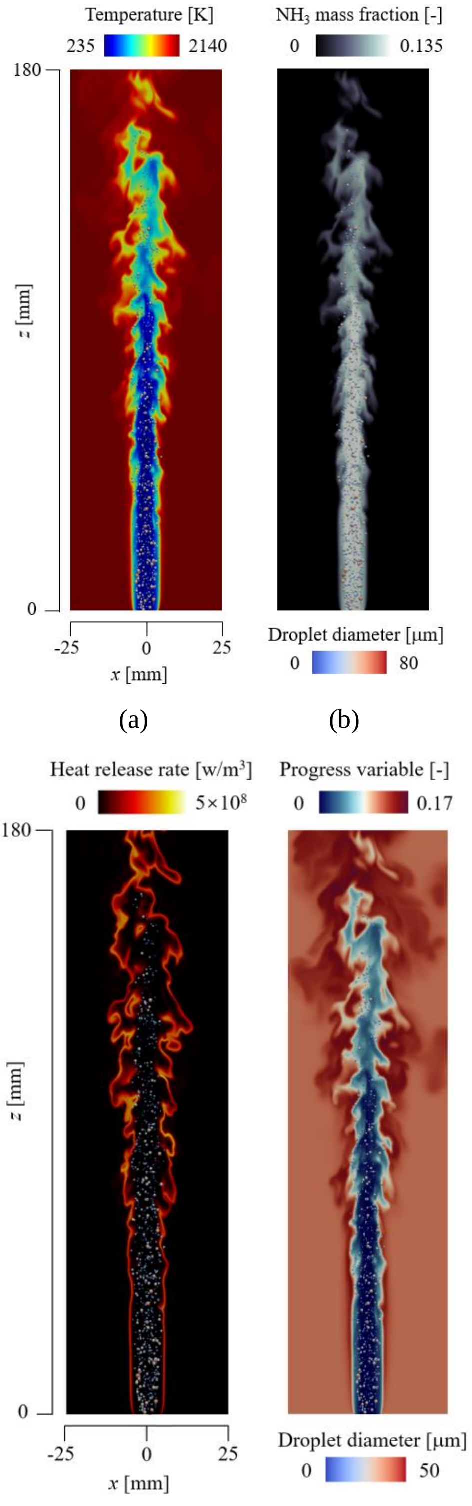

(a) (b)

(c) (d)

Fig. 8. Instantaneous distributions of (a) gas phase temperature, (b) NH_3 mass fraction, (c) HRR, and (d) progress variable at $t = 8$ ms. The droplets are shown as dots, and their sizes are determined by the relative diameters.

Figure 8 (c) presents the Heat Release Rate (HRR) field. Due to the presence of the high-temperature co-flow, heat release occurs immediately at the fuel outlet. However, the flash evaporation rate is the highest in this region, and the phase transition absorbs a substantial amount of heat, resulting in relatively low HRR at this location. From upstream to downstream locations, the HRR gradually increases. In the downstream region, turbulence causes more flame wrinkling, and the combined effects of turbulence and reduced heat absorption from phase transitions lead to localized increases in HRR. On the other hand, due to the presence of droplets, the HRR distribution becomes increasingly uneven further downstream. In certain local regions, the HRR is very low, while the combined effects of turbulence and droplets create isolated zones of high HRR, forming HRR islands within the flame structure. Figure 8 (d) shows the progress variable represented by the mass fraction of H_2O. This variable serves as an indicator of the combustion progress, where higher values correspond to regions with more advanced reactions. Near the fuel outlet, the progress variable remains relatively low due to the dominance of evaporation and mixing processes. As the flow moves downstream, the progress variable increases steadily, indicating the onset and intensification of reaction. The high temperature and low-oxygen environment provide conditions for stable combustion of liquid ammonia. To determine the complete combustion, Fig. 9 shows the mass fraction of unburned NH_3 and NO_2 at the chamber exit.

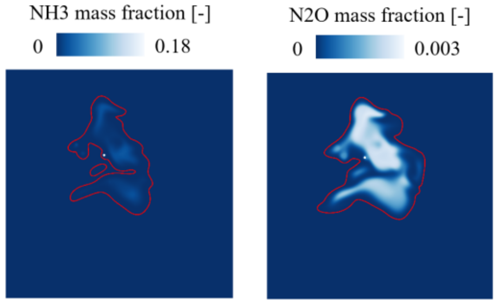

(a) (b)

Fig. 9. Mass fraction of (a) unburned NH_3 and (b) NO_2 at the chamber exit. The red iso-lines represent the temperature value of 2000 K.

In previous studies on premixed ammonia flames, the phenomenon of reaction zone thickening was observed [42,43], and it was found that the thickening of the reaction zone is a spatially evolving process. Figure 10 shows the distribution of NH mass fraction on the horizontal cross-sections at $z = 20, 80, 160$ mm. The NH layer is shown by red iso-lines. The relative size of the droplets is represented by white dots. There is consistently a significant gap between the droplet region and the reaction zone. The wrinkling of the reaction zone is primarily influenced by turbulent vortex structures generated by jet shear. In the upstream region, vortices cannot penetrate the reaction zone, preventing it from thickening. The NH layer thickness resembles that of a laminar flame, and thus, near the nozzle, the flame remains almost wrinkle-free. This is because only vortices with a scale larger than the laminar flame thickness can wrinkle the flame [44]. Near the burner nozzle, the vortices are confined within the length scale of the nozzle diameter. As the flow develops downstream, the jet expands radially, increasing the reaction zone diameter. Concurrently, detached, independent reaction zone structures emerge, separated from the main flow.

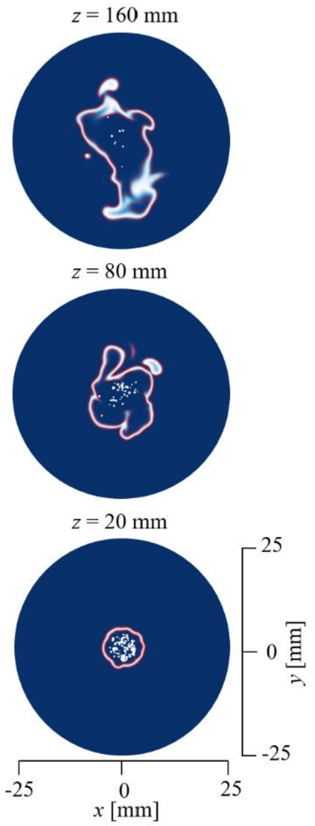

Fig. 10. Distribution of NH mass fraction on the horizontal cross-sections at z = 20, 80, 160 mm. The NH layer is shown by red iso-lines. The red iso-lines represent the NH mass fraction value of 1.2×10^{-5}.

To further quantitatively describe the variation in the average thickness of the NH layer, Fig. 11 shows the mean relative NH layer thickness and its standard deviation along z-axial. It can be observed that, beyond z = 40 mm, the thickness of the NH layer begins to increase significantly, reaching 2.5 times its initial value at z = 160 mm. This thickening ratio is comparable to that of the Lund University Piloted Jet flame with a Karlovitz number of 581 [43]. The phenomenon of reaction zone thickening in liquid ammonia jet flames is very similar to that observed in premixed ammonia jet flames. This similarity arises from the intense flash boiling of liquid ammonia within the Lr region and the complete flash evaporation before to reaction, resulting in flame characteristics closely resembling those of premixed ammonia flames.

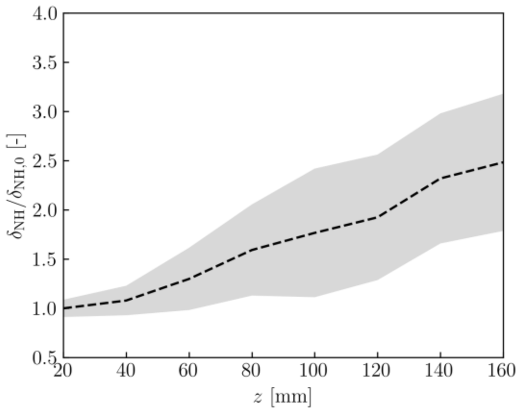

Fig. 11. Mean relative NH layer thickness and its standard deviation at different height.

5. Conclusions

A liquid ammonia jet flame was studied using experimental measurements and simulations. The experiment provided statistical data on the spray characteristics close to nozzle. The quasi-DNS coupled detailed chemistry was employed to further investigate the liquid ammonia jet flame structure. The boundary conditions and inlet parameters for the simulations were derived from the experiment, and the droplet field was compared with the experimental data for validation. Main conclusions were summarized as follows:

1. The experimental results indicated that intense atomization and evaporation of liquid ammonia occurred within the 6.5 mm recess length region, forming a well-atomized spray before injection. Only 22.8% of the ammonia entered the combustion region in the liquid phase, and the droplets had relatively small mean diameters.
2. The simulation results were validated against experimental data and showed good agreement. The simulated flame structure revealed that, due to flash evaporation, the axial temperature of the flame was extremely low, with droplets mainly distributed in the low temperature region. In the burned region, droplets were

almost absent as they had almost completely evaporated before crossing the flame front.

3. The simulation results showed that the liquid ammonia jet flame exhibited the phenomenon of reaction zone thickening from upstream to downstream, similar to that observed in typical ammonia flames.

Acknowledgments

This work was partially supported by MEXT as "Program for Promoting Researches on the Supercomputer Fugaku" (Development of the Smart design system on the supercomputer "Fugaku" in the era of Society 5.0) (JPMXP1020210316). This research used the computational resources of supercomputer Fugaku provided by the RIKEN Center for Computational Science (Project ID: hp230258 and hp230321). Z.H.A is grateful to China Scholarship Council (Project No. 202206280012). J.K.X and R.K especially thank the support from Japan Society for the Promotion of Science (Grant No: 21P20351).

Conflicts of Interest

The authors declare that they have no known competing financial interests or personal relationships that could have appeared to influence the work reported in this paper.

References

[1] Valera-Medina A, Xiao H, Owen-Jones M, David WI, Bowen PJ. Ammonia for power. Prog Energy Combust Sci 2018;69:63–102.https://doi.org/10.1016/j.pecs.2018.07.001

[2] Kobayashi H, Hayakawa A, Somarathne KKA, Okafor EC. Science and technology of ammonia combustion. Proc Combust Inst 2019;37:109–33. https://doi.org/10.1016/j.proci.2018.09.029

[3] Valera-Medina A, Amer-Hatem F, Azad AK, Dedoussi IC, De Joannon M, Fernandes RX, et al. Review on ammonia as a potential fuel: from synthesis to economics. Energy Fuels 2021;35:6964–7029. https://doi.org/10.1021/acs.energyfuels.0c03685

[4] Zhang M, Wei X, An Z, Okafor EC, Guiberti TF, Wang J, et al. Flame stabilization and emission characteristics of ammonia combustion in lab-scale gas turbine combustors: Recent progress and prospects. Prog Energy Combust Sci 2025;106:101193. https://doi.org/10.1016/j.pecs.2024.101193

[5] Hayakawa A, Goto T, Mimoto R, Arakawa Y, Kudo T, Kobayashi H. Laminar burning velocity and Markstein length of ammonia/air premixed flames at various pressures. Fuel 2015;159:98–106. https://doi.org/10.1016/j.fuel.2015.06.070.

[6] Wei X, Zhang M, An Z, Wang J, Huang Z, Tan H. Large eddy simulation on flame topologies and the blow-off characteristics of ammonia/air flame in a model gas turbine combustor. Fuel 2021;298:120846. https://doi.org/10.1016/j.fuel.2021.120846

[7] Valera-Medina A, Marsh R, Runyon J, Pugh D, Beasley P, Hughes T, et al. Ammonia–methane combustion in tangential swirl burners for gas turbine power generation. Appl Energy 2017;185:1362–71. https://doi.org/10.1016/j.apenergy.2016.02.073 https://doi.org/10.1016/j.apenergy.2016.02.073.

[8] An Z, Zhang M, Zhang W, Mao R, Wei X, Wang J, et al. Emission prediction and analysis on CH4/NH3/air swirl flames with LES-FGM method. Fuel 2021;304:121370. https://doi.org/10.1016/j.fuel.2021.121370

[9] Valera-Medina A, Gutesa M, Xiao H, Pugh D, Giles A, Goktepe B, et al. Premixed ammonia/hydrogen swirl combustion under rich fuel conditions for gas turbines operation. Int J Hydrog Energy 2019;44:8615–26. https://doi.org/10.1016/j.ijhydene.2019.02.041

[10] Wei X, Zhang M, Wang J, Huang Z. Investigation on lean blow-off characteristics and stabilization mechanism of premixed hydrogen enhanced ammonia/air swirl flames in a gas turbine combustor. Combust Flame 2023;249:112600. https://doi.org/10.1016/j.combustflame.2022.112600

[11] Xing J, Pillai AL, Kurose R. Heat release rate surrogate for ammonia–hydrogen premixed flames under various conditions. Appl Energy Combust Sci 2023;15:100193. https://doi.org/10.1016/j.jaecs.2023.100193

[12] Hayakawa A, Arakawa Y, Mimoto R, Somarathne KDKA, Kudo T, Kobayashi H. Experimental investigation of stabilization and emission characteristics of ammonia/air premixed flames in a swirl combustor. Int J Hydrog Energy 2017;42:14010–8. https://doi.org/10.1016/j.ijhydene.2017.01.046

[13] Xin G, Ji C, Wang S, Hong C, Meng H, Yang J. Experimental study on the effect of hydrogen substitution rate on combustion and emission characteristics of ammonia internal combustion engine under different excess air ratio. Fuel 2023;343:127992. https://doi.org/10.1016/j.fuel.2023.127992

[14] Novella R, Pastor J, Gomez-Soriano J, Sánchez-Bayona J. Numerical study on the use of ammonia/hydrogen fuel blends for automotive spark-ignition engines. Fuel 2023;351:128945. https://doi.org/10.1016/j.fuel.2023.128945

[15] An Z, Xing J, Kurose R. Recent progresses in research on liquid ammonia spray and combustion: A review. Appl Energy Combust Sci 2024;20:100293. https://doi.org/10.1016/j.jaecs.2024.100293

[16] Okafor EC, Kurata O, Yamashita H, Inoue T, Tsujimura T, Iki N, et al. Liquid ammonia spray combustion in two-stage micro gas turbine combustors at 0.25 MPa; Relevance of combustion enhancement to flame stability and NOx control. Appl Energy Combust Sci 2021;7:100038. https://doi.org/10.1016/j.jaecs.2021.100038

[17] Pelé R, Mounaïm-Rousselle C, Bréquigny P, Hespel C, Bellettre J. First Study on Ammonia Spray Characteristics with a Current GDI Engine Injector. Fuels 2021;2:253–71. https://doi.org/10.3390/fuels2030015.

[18] Payri R, García JM, Salvador FJ, Gimeno J. Using spray momentum flux measurements to understand the influence of diesel nozzle geometry on spray characteristics. Fuel 2005;84:551–61. https://doi.org/10.1016/j.fuel.2004.10.009

[19] Li S, Li T, Wang N, Zhou X, Chen R, Yi P. An investigation on near-field and far-field characteristics of superheated ammonia spray. Fuel 2022;324. https://doi.org/10.1016/j.fuel.2022.124683

[20] Li T, Zhou X, Wang N, Wang X, Chen R, Li S, et al. A comparison between low- and high-pressure injection dual-fuel modes of diesel-pilot-ignition ammonia combustion engines. J Energy Inst 2022;102:362–73. https://doi.org/10.1016/j.joei.2022.04.009

[21] Xu L, Dong P, Zhang Z, Bu J, Tian J, Long W, et al. Impact of spray interaction on ammonia/diesel dual-fuel combustion and emission under engine relevant conditions. Proc Combust Inst 2024;40:105751. https://doi.org/10.1016/j.proci.2024.105751

[22] Zhou X, Li T, Wang N, Wang X, Chen R, Li S. Pilot diesel-ignited ammonia dual fuel low-speed marine engines: A comparative analysis of ammonia premixed and high-pressure spray combustion modes with CFD simulation. Renew Sustain Energy Rev 2023;173:113108. https://doi.org/10.1016/j.rser.2022.113108

[23] An Z, Xing J, Kurose R. Numerical study on the phase change and spray characteristics of liquid ammonia flash spray. Fuel 2023;345. https://doi.org/10.1016/j.fuel.2023.128229

[24] Huang Z, Wang H, Luo K, Fan J. Large eddy simulation investigation of ammonia spray characteristics under flash and non-flash boiling conditions. Appl Energy Combust Sci 2023;16. https://doi.org/10.1016/j.jaecs.2023.100220.

[25] Shin J, Park S. Numerical analysis for optimizing combustion strategy in an ammonia-diesel dual-fuel engine. Energy Convers Manag 2023;284. https://doi.org/10.1016/j.enconman.2023.116980

[26] Zhang Y, Xu L, Zhu Y, Xu S, Bai X-S. Numerical study on liquid ammonia direct injection spray characteristics under engine-relevant conditions. Appl Energy 2023;334. https://doi.org/10.1016/j.apenergy.2023.120680

[27] Wang R, An Z, Zhang M, Chen J, Cai X, Wang J, et al. The two-phase characteristics of liquid ammonia jet spray flame in a hot and low oxygen coflow. Combust Flame Under Review.

[28] Hayakawa A, Goto T, Mimoto R, Kudo T, Kobayashi H. NO formation/reduction mechanisms of ammonia/air premixed flames at various equivalence ratios and pressures. Mech Eng J 2015;2:14-00402-14–00402. https://doi.org/10.1299/mej.14-00402

[29] Wang R, Zhang M, An Z, Cai X, Liu J, Wang J, et al. Topology characteristics of liquid ammonia swirl spray flame. Proc Combust Inst 2024;40. https://doi.org/10.1016/j.proci.2024.105740

[30] Evrard F, Denner F, Van Wachem B. Quantifying the errors of the particle-source-in-cell Euler-Lagrange method. Int J Multiph Flow 2021;135:103535. https://doi.org/10.1016/j.ijmultiphaseflow.2020.103535

[31] Xing J, Luo K, Wang H, Jin T, Cai R, Fan J. A DNS study on temporally evolving jet flames of pulverized coal/biomass co-firing with different blending ratios. Proc Combust Inst 2021;38:4005–12. https://doi.org/10.1016/j.proci.2020.06.007

[32] Miller RS, Bellan J. Direct numerical simulation of a confined three-dimensional gas mixing layer with one evaporating hydrocarbon-droplet-laden stream. J Fluid Mech 1999;384:293–338. https://doi.org/10.1017/S0022112098004042

[33] Xing J, An Z, Kurose R. Analysis and flamelet modeling of preferential evaporation in SAF/Jet A spray flames. Proc Combust Inst 2024;40:105707. https://doi.org/10.1016/j.proci.2024.105707

[34] Ranz W, Marshall W. Evaporation from droplets. Chem Eng Prog 1952;48:41–146.

[35] Reitz RD, Diwakar R. Effect of drop breakup on fuel sprays. SAE Trans 1986:218–27. https://www.jstor.org/stable/44725372

[36] Price C, Hamzehloo A, Aleiferis P, Richardson D. Aspects of Numerical Modelling of Flash-Boiling Fuel Sprays. Warrendale, PA: SAE International; 2015. https://doi.org/10.4271/2015-24-2463

[37] An Z, Xing J, Pillai AL, Kurose R. Numerical study on spherical flame propagation in dispersed liquid ammonia droplets. Fuel 2024;357. https://doi.org/10.1016/j.fuel.2023.129660

[38] Issa RI. Solution of the implicitly discretised fluid flow equations by operator-splitting. J Comput

Phys 1986;62:40–65. https://doi.org/10.1016/0021-9991(86)90099-9

[39] Thomas LM, Lowe A, Satija A, Masri AR, Lucht RP. Five kHz thermometry in turbulent spray flames using chirped-probe pulse femtosecond CARS, part I: Processing and interference analysis. Combust Flame 2019;200:405–16. https://doi.org/10.1016/j.combustflame.2018.11.004

[40] Lowe A, Thomas LM, Satija A, Lucht RP, Masri AR. Five kHz thermometry in turbulent spray flames using chirped-probe-pulse femtosecond CARS, part II: Structure of reaction zones. Combust Flame 2019;200:417–32. https://doi.org/10.1016/j.combustflame.2018.10.034

[41] Proud DB, Evans MJ, Medwell PR, Chan QN. Experimental investigation of the flame structure of dilute sprays issuing into a hot and low-oxygen coflow. Combust Flame 2021;230:111439. https://doi.org/10.1016/j.combustflame.2021.111439

[42] Zhou B, Brackmann C, Li Z, Aldén M, Bai X-S. Simultaneous multi-species and temperature visualization of premixed flames in the distributed reaction zone regime. Proc Combust Inst 2015;35:1409–16. https://doi.org/10.1016/j.proci.2014.06.107

[43] Xu L, Fan Q, Liu X, Cai X, Subash AA, Brackmann C, et al. Flame/turbulence interaction in ammonia/air premixed flames at high karlovitz numbers. Proc Combust Inst 2023;39:2289–98. https://doi.org/10.1016/j.proci.2022.09.010

[44] Peters N. Turbulent Combustion. Meas Sci Technol 2001;12:2022. https://doi.org/10.1088/0957-0233/12/11/708